



Cite this: *Chem. Commun.*, 2017, **53**, 5204

Received 24th December 2016,
Accepted 18th April 2017

DOI: 10.1039/c6cc10208e

rsc.li/chemcomm

Diamondoid-structured polymolybdate-based metal–organic frameworks as high-capacity anodes for lithium-ion batteries†

Yuan-Yuan Wang,^{‡a} Mi Zhang,^{‡b} Shun-Li Li,^b Shu-Ran Zhang,^a Wei Xie,^a
Jun-Sheng Qin,^a Zhong-Min Su^{id} ^{*a} and Ya-Qian Lan^{id} ^{*ab}

Two novel isostructural polyoxometalate (POM)-based metal–organic frameworks (MOFs) with diamond topology, NENU-506 and NENU-507, were hydrothermally synthesized. They not only combine the advantages of both POMs and MOFs, but also show excellent chemical and thermal stability. Notably, NENU-507 exhibited a high reversible capacity of 640 mA h g^{−1} after 100 cycles when applied as an anode material in lithium-ion batteries.

Lithium-ion batteries (LIBs) are expected to be one of the most promising power sources for hybrid electric vehicles (HEVs) and electric vehicles (EVs) owing to their high energy density, light weight and environmental friendliness.¹ Therefore, tremendous efforts have been devoted to the development of anode materials with superior performance to meet the increasingly demanding requirements for energy storage.² To date, graphite has been widely utilized as a commercial anode material, but it suffers from a limited theoretical capacity (372 mA h g^{−1}) and poor rate performance.³ Several kinds of alternatives for anode materials have been reported, such as metal oxides,⁴ Sn-based composites,⁵ P-based composites,⁶ Si-based composites,⁷ *etc.* However, their coulombic efficiency and cycling stability have been hampered by the undesirable large volume change. As a consequence, the investigation of anode materials with high reversible capacity and excellent structural stability is highly desirable for LIBs.

During the past two decades, research on porous MOFs has rapidly developed in the fields of gas storage and separation,

catalysis, sensor, drug delivery, and so on, due to their high porosity and chemically tunable structures.⁸ In particular, pure MOFs have been investigated as attractive anode materials for LIBs, which highlight the importance of host architectures allowing rapid insertion of species. MOF-177, directly used as an anode material for LIBs, was first investigated in 2006. The pioneering work was not satisfactory and had considerable drawbacks, for instance, limited initial discharge capacity and rapid cell failure, but this work has led to the continual discovery of new MOF materials as anodes for LIBs with better performance.⁹ A systematic investigation on the electrochemical performance of diamondoid-structured Zn₃(HCOO)₆ revealed that an invariable capacity of close to 560 mA h g^{−1} was obtained up to 60 cycles at 60 mA g^{−1}.¹⁰ After that, a highly porous and crystalline MOF (Cu-BDC) as the anode material in LIBs delivered 227 mA h g^{−1} in the first cycle, which is approximately 95% of the theoretical capacity.¹¹ Recently, although several MOFs have been applied in LIBs, these materials display limited capacity or poor cycling performance, resulting from their decomposition in the first several cycles.¹²

POMs are mostly soluble anionic metal oxide clusters with oxygen-rich surfaces. In the process of reversible multielectron redox transformations, POMs can maintain their unmatched structure under rather mild conditions, which have attracted particular interest in areas such as medicine, biology, magnetism, materials science and catalysis.¹³ POM-based MOF materials, combining the advantages of both POMs and MOFs, have been the focus of considerable interest due to their fascinating structures and intriguing properties. The redox of metal ions inside POMs is favorable for the insertion/extraction of Li⁺. Furthermore, the open framework structure of MOFs has been proved to be an effective way of strengthening the cycling stability, which will overcome the disadvantages of large volume change during lithium insertion/extraction. Dai *et al.* synthesized a POMOF material based on {Ni₆PW₉} structural building units (SBUs) and rigid carboxylate linkers and used it as an anode material.¹⁴ It is apparent to note that the development of POMOF materials utilized as anode materials in LIBs is still at its early stage.

^a Institute of Functional Material Chemistry, Faculty of Chemistry, Northeast Normal University, Changchun 130024, Jilin, People's Republic of China.
E-mail: zmsu@nenu.edu.cn, yqlan@nenu.edu.cn

^b Jiangsu Key Laboratory of Biofunctional Materials, School of Chemistry and Materials Science, Nanjing Normal University, Nanjing 210023, Jiangsu, People's Republic of China

† Electronic supplementary information (ESI) available: TGA, XPRD patterns, IR, UV data and additional figures. CCDC 1491390 and 1491371. For ESI and crystallographic data in CIF or other electronic format see DOI: 10.1039/c6cc10208e

‡ These authors contribute equally.

In this communication, we reported two tetrahedrally connected networks comprising ϵ -Keggin polymolybdate units capped by four Zn ions linked through linear rigid bifunctional ligands, possessing an interpenetrated diamond topology, successfully, namely, $(\text{TBA})_3[\text{PMo}_8^{\text{V}}\text{Mo}_4^{\text{VI}}\text{O}_{38}(\text{OH})_2\text{Zn}_4(\text{IN})_2]$ (**NENU-506**; IN = isonicotinic acid, TBA^+ = tetrabutylammonium ion) and $(\text{TBA})_3[\text{PMo}_8^{\text{V}}\text{Mo}_4^{\text{VI}}\text{O}_{38}(\text{OH})_2\text{Zn}_4(\text{PBA})_2] \cdot \text{H}_2\text{O}$ (**NENU-507**; HPBA = 4-(pyridin-4-yl) benzoic acid). To the best of our knowledge, POMOFs based on Zn- ϵ -Keggin units and bifunctional ligands have not been reported so far, which is an encouraging step towards the synthesis of a new family of POMOFs.¹⁵ Owing to the different lengths of linkers, the diamond network as a typical interpenetrating topology may possess the characteristics of “self-recognition”.¹⁶ Furthermore, **NENU-507** was directly utilized as an anode material for LIBs, maintaining the three-dimensional (3D) rigid structure during lithiation/delithiation cycles, owing to its excellent chemical and thermal stability (as shown in Table S6, ESI†). The Zn- ϵ -Keggin units as variable-valence metal clusters exhibited reversible redox activity. Meanwhile, the open framework structure of MOFs enables the accommodation of large volume changes during cycling at relatively high current rates. Within the voltage window of 0.01–3.0 V, the POM-based MOF electrode material showed an outstanding reversible specific capacity of 640 mA h g^{−1} at a current density of 100 mA g^{−1} over 100 cycles. As expected, the unique pore structure is beneficial for efficient and reversible insertion and extraction of Li⁺ ions.

Single-crystal X-ray diffraction analysis reveals that **NENU-506** (Fig. 1a) crystallizes in the space group of *Pbcn* (Table S1, ESI†). The connectivity between ϵ -type Keggin polyoxometalates and IN ligands leads to a highly porous extended 3D framework. The asymmetric unit contains one $[\epsilon\text{-PMo}_8^{\text{V}}\text{Mo}_4^{\text{VI}}\text{O}_{36}(\text{OH})_4\text{Zn}_4]^+$ ion, two IN ligands, and three TBA^+ cations (Fig. S4, ESI†). In **NENU-506**, each capping Zn^{2+} ion in the tetrahedral environment is bound to three oxygen atoms of the Keggin cluster unit, and the remaining coordination site is occupied by a nitrogen atom or a one oxygen atom of two different IN ligands. As expected, the ϵ -Keggin ion is an eight-electron-reduced POM unit. Examination of the Mo–Mo distances has confirmed the presence of eight Mo(V) and four Mo(VI) ions in **NENU-506** (Fig. S5, ESI†). The assignment of the oxidation states is apparent from the results of bond valence sum (BVS) calculations on the Mo centers (Table S4, ESI†) and X-ray photoelectron spectroscopy (XPS) analysis (Fig. S7, ESI†). Therefore, from the point view of topology, each ϵ -Keggin polymolybdate unit capped by four Zn ions can be viewed as a tetrahedral node, which tends to connect with four crystallographically equivalent units to form a characteristically three-dimensional *dia* network. A more interesting feature here is that the single network has large open channels along the crystallographic *c*-axis (Fig. 1b and c). For the purpose of increasing the stability of the framework and avoiding the formation of large open channels, the single network is penetrated by another identical *dia* network to generate a two-fold interpenetrated diamond array (Fig. 1d). As shown below in Fig. S13 (ESI†), an infinite helical chain is composed of the tetrahedral nodes bridged by a linear rigid bifunctional ligand that runs along the *a*-axis. There are two infinite helical chains from two individual diamondoid nets entangled each other in **NENU-506**.

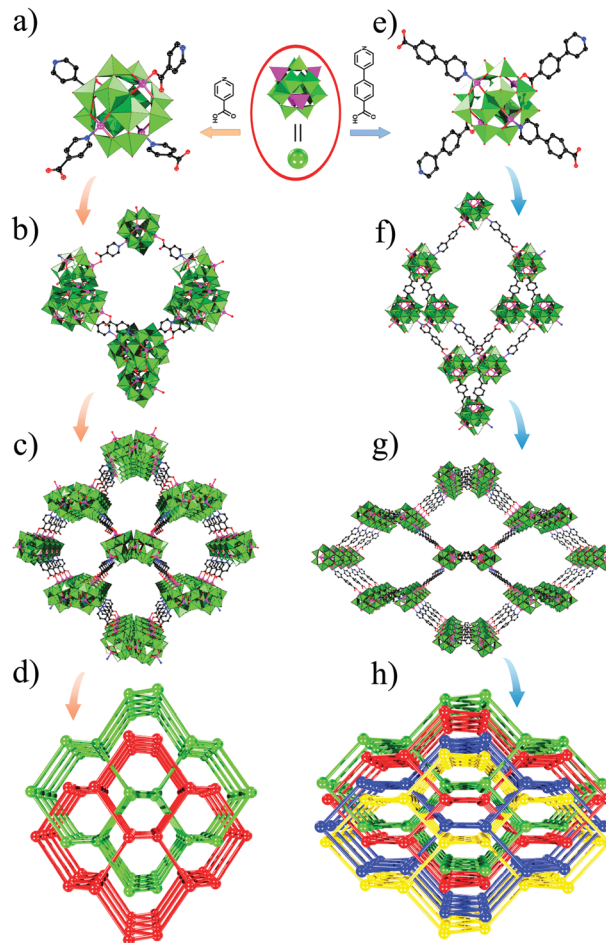


Fig. 1 Summary of the structures of **NENU-506** and **NENU-507**: (a and e) connection mode between Zn- ϵ -Keggin and IN[−] and PBA[−] fragments, respectively; (b and f) the single adamantanoid cages in **NENU-506** and **NENU-507**, respectively; (c and g) 3D frameworks of **NENU-506** and **NENU-507**, respectively; and (d and h) two-fold and four-fold interpenetrated *dia* arrays, respectively.

The substitution of the IN ligand by a HPBA ligand under similar conditions yielded **NENU-507** (Fig. 1e). **NENU-507** crystallizes in the tetragonal space group *I4₁/acd* (Table S1, ESI†). Two adjacent ϵ -Keggin units were linked by a HPBA ligand which served as a linear bridge, leading to the formation of a 3D open-framework, whose channels are occupied by TBA^+ cations. As expected, the coordination environments of Zn^{2+} ions in **NENU-507** are similar to those in **NENU-506**. The BVS calculations affirmed that the electrons of the ϵ -Keggin unit in **NENU-507** are highly delocalized on account of the high symmetry (Table S5, ESI†). **NENU-507** is dark red (Fig. S9, ESI†), which is the typical color of reduced molybdenum blue species¹⁷ and is in agreement with the XPS analysis (Fig. S7, ESI†). When using longer HPBA ligands instead of IN ligands, **NENU-507** with a spacious nature of the single network was obtained, resulting in a four-fold interpenetrated diamond network (Fig. 1g and h). The interlaced scanning system is regarded as the most attractive feature of the 4-fold-interpenetrated network. Four helical chains from four individual *dia* nets can be considered as two

pairs of helices of opposite helicity, which is different from a conventional double helix. The association between the two independent single-stranded helices represents a side-by-side polymeric double helix (Fig. S14, ESI†). Although the X-ray diffraction cannot determine the positions of TBA⁺ cations, the fact is that TBA⁺ cations have the ability to compensate the remaining charges.

As previously mentioned, high chemical and thermal stability of electrode materials is absolutely crucial. Powder X-ray diffraction (PXRD) patterns of **NENU-506** and **NENU-507** between the as-synthesized samples and the simulated ones reveal their crystalline phase purity (Fig. S1, ESI†). As shown in Fig. 2a and b, **NENU-507** shows great tolerance to acid/base aqueous solutions at room temperature with a wide pH range of 2–12, which is also confirmed by the Fourier transformed infrared spectroscopy (FT-IR) measurements (Fig. S10, ESI†). Additionally, **NENU-507** is also stable after soaking in common organic solvents (such as dimethylacetamide (DMA), dimethylformamide (DMF), methanol (MeOH), or ethanol (EtOH)) for 3 days at room temperature (Fig. S11, ESI†). **NENU-507** can well maintain its crystallinity when immersed in electrolytes used for LIBs (Fig. S15, ESI†).

The thermal stability of **NENU-506** and **NENU-507** has been measured by thermogravimetric analysis (TGA) in a dry nitrogen atmosphere. The TGA curve of **NENU-506** (Fig. S3, ESI†) reveals the first step of weight loss immediately occurred upon heating before the temperature reached 120 °C, due to the loss of all lattice water molecules. From 275 to 570 °C, the whole framework collapses with the release of all organic ligands, guest molecules, and TBA⁺ ions. The TGA curve of **NENU-507** reveals a continuous weight loss step from 300 to 570 °C, which belongs to the removal of organic ligands and TBA⁺ ions. The PXRD patterns of the samples heated in flowing N₂ further demonstrate that **NENU-506** and **NENU-507** display good thermal stabilities by retaining their structural integrity up to 250 and 275 °C, respectively (Fig. S6b and S11b, ESI†).

The successful fabrication of stable crystalline porous POM-based MOF materials for a LIB anode is evident based on the superior electrochemical performance. In order to gain further insight into the reaction mechanism during charge-discharge processes, cyclic voltammetry (CV) experiments were

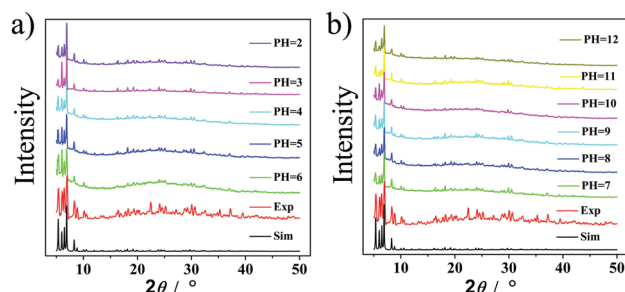


Fig. 2 PXRD patterns of **NENU-507**, with the as-synthesized sample immersed in water with different pH values at room temperature for 24 h. "Sim" represents the simulated pattern, and "Exp" represents the pattern of the as-synthesized sample.

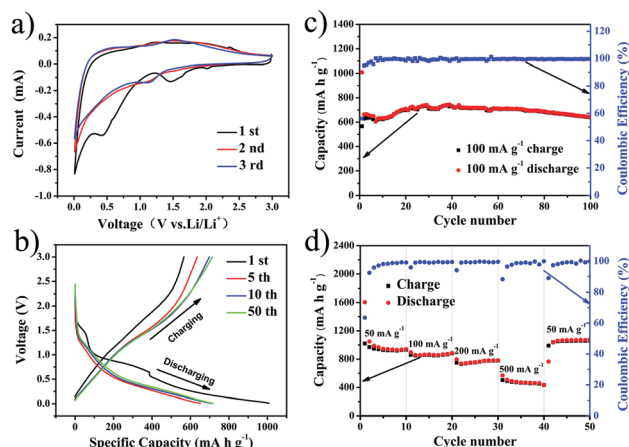


Fig. 3 Electrochemical performance of the **NENU-507** electrode: (a) CV curves at a scan rate of 0.2 mV s⁻¹ in the voltage window of 0.01–3.0 V vs. Li/Li⁺; (b) Galvanostatic charge-discharge voltage curves of the selected cycles; (c) long cycling performance at a current density of 100 mA g⁻¹; and (d) rate performance at different current densities from 50 to 500 mA g⁻¹.

carried out and the results are illustrated in Fig. 3a. In the first cycle, a well-defined cathodic peak was observed at about 0.47 V, which can be associated with the formation of a solid-electrolyte interphase (SEI) film.¹⁸ Owing to the first process of inserting Li⁺ ions, the distinct reduction peaks can be seen at 1.48 V. However, as the corresponding oxidation peaks are, if existent, significantly less pronounced, these processes are largely irreversible. Subsequently, the reversibility of the reductive peak at 1.15 V and the oxidative peak at 1.52 V was observed, which may be assigned to the reduction and oxidation of Zn and Mo, respectively (XPS results in Fig. S17, ESI†).¹⁹ The CV curves of the following cycles almost overlap with each other, indicating the excellent cycling stability of the **NENU-507** electrode. These results are also consistent with the galvanostatic charge-discharge profiles. Fig. 3b shows the discharge/charge profiles of the selected cycles at a low current density of 100 mA g⁻¹. The discharge curve in the first cycle is as high as 1008 mA h g⁻¹, while its first reversible specific capacity is only 566 mA h g⁻¹, giving rise to an initial coulombic efficiency of approximately 56.15%. The relative low initial coulombic efficiency can be ascribed to the irreversible capacity loss, including the formation of the SEI film and the decomposition of the electrolyte. Apart from the first discharge curve, the capacity remains stable, highlighting the excellent cycling stability and reversibility of **NENU-507** as a high-performance anode material.

The cycling performance of **NENU-507** was investigated at a current density of 100 mA g⁻¹ over the range of 0.01–3.0 V versus Li/Li⁺. As shown in Fig. 3c, **NENU-507** showed excellent cycling stability with high capacity. After 100 cycles, the electrode still maintained a discharge capacity of 640 mA h g⁻¹, which is approximately 96.68% of that of the second electrode (662 mA h g⁻¹). Apparently, the coulombic efficiency increased dramatically to nearly 100% after seven cycles and was maintained even after 100 cycles. The rate performance, as one of the pre-requisite for lithium-ion battery electrodes, was investigated at various current densities (from 50 to 500 mA g⁻¹)

and the results are illustrated in Fig. 3d. When the current density gradually increased from 50 to 100, 200 and 500 mA g⁻¹, the corresponding average discharge capacities decreased from 1024 to 868, 767 and 480 mA h g⁻¹, respectively. Even at a high current rate of 500 mA g⁻¹, **NENU-507** achieved a reversible capacity of 480 mA h g⁻¹, which is much higher than that of graphite (430 mA h g⁻¹). When the current rate became 50 mA g⁻¹ again, the material exhibited the same reversible capacity of approximately 1034 mA h g⁻¹, indicating a good cycling performance.

For comparison, the cycling performance of **NENU-506** was also tested (Fig. S16, ESI†). Considering **NENU-507** showed higher reversible capacity and better cycling stabilities, **NENU-507** was used for further characterization studies in order to explore the reaction mechanism. In contrast to traditional electrode materials, the open framework **NENU-507** anode material contained variable-valence metal cluster SBUs. Interestingly, the discharge and charge capacities of the **NENU-507** electrode are much higher than the expected theoretical value (233 mA h g⁻¹, detailed information in ESI,† S4), which may be contributed by the capacitive behavior.²⁰ The element valences of **NENU-507** before and after LIB cycling were confirmed using XPS results (Fig. S17, ESI†). The Mo 3d spectrum (Fig. S17c, ESI†) of **NENU-507** shows four peaks at 235.2, 232.1, 243.3 and 231.2 eV, which can be ascribed to Mo⁶⁺ 3d_{3/2}, Mo⁶⁺ 3d_{5/2}, Mo⁵⁺ 3d_{3/2} and Mo⁵⁺ 3d_{5/2}, respectively. However, the binding energy of 232.2 eV demonstrates the existence of Mo⁴⁺ after discharging to 0.01 V as can be seen in Fig. S17g (ESI†), which confirms the redox reaction of Mo in [ε-PMo₈Mo₄^{VI}O₃₆(OH)₄Zn₄]⁺ ions.²¹ In Fig. S17d (ESI†), the two peaks located at 1044.7 and 1021.7 eV can be assigned to Zn 2p_{1/2} and 2p_{3/2}, respectively, which reveals the ionic state of Zn in **NENU-507** samples before lithium take-up. After discharging to 0.01 V, both the shift in binding energy and the increase in the separation of the binding energy imply the formation of metallic zinc during the electrochemical reactions (Fig. S17h, ESI†).⁹ To further investigate the electrochemical performance of **NENU-507**, scanning electron microscopy (SEM) analyses were used to observe the morphology changes of the electrode after 50 cycles performed at a current density of 500 mA g⁻¹. As shown in Fig. S18 (ESI†), there is no significant difference in the morphology, indicating the stability of the electrode. Based on the discussion above, the battery behavior of **NENU-507** is achieved by coordination with Li in the organic moiety and redox of metal ions (Mo and Zn).

In summary, we have constructed two unprecedented, highly stable POM-based MOFs using a hydrothermal method. For the first time, the Zn-ε-Keggin units acting as nodes were directly connected by two bifunctional ligands to form two 3D open frameworks. In contrast to most POM-based MOFs, these two compounds exhibit excellent chemical and thermal stabilities. Meanwhile, **NENU-507**, when directly applied as an anode material for LIBs, delivered a reversible capacity of 640 mA h g⁻¹ after

100 cycles at a current density of 100 mA g⁻¹. This material exhibited impressive rate capability, high reversible capacity, and superior cycling performance, which will open new possibilities for utilizing POM-based MOFs as electrode materials in LIBs.

This work was financially supported by the National Natural Science Foundation of China (No. 21622104, 21371099 and 21471080), the NSF of Jiangsu Province of China (No. BK20141445), the Priority Academic Program Development of Jiangsu Higher Education Institution and the Foundation of Jiangsu Collaborative Innovation Center of Biomedical Functional Materials.

Notes and references

- 1 D. Larcher and J. Tarascon, *Nat. Chem.*, 2014, **7**, 19–29.
- 2 S. J. Yang, S. Nam, T. Kim, J. H. Im, H. Jung, J. H. Kang, S. Wi, B. Park and C. R. Park, *J. Am. Chem. Soc.*, 2013, **135**, 7394–7397.
- 3 L. Zhang, H. B. Wu, S. Madhavi, H. H. Hng and X. W. Lou, *J. Am. Chem. Soc.*, 2012, **134**, 17388–17391.
- 4 D. Ge, H. Geng, J. Wang, J. Zheng, Y. Pan, X. Cao and H. Gu, *Nanoscale*, 2014, **6**, 9689–9694.
- 5 P. V. Prikhodchenko, D. Y. W. Yu, S. K. Batabyal, V. Uvarov, J. Gun, S. Sladkevich, A. A. Mikhaylov, A. G. Medvedev and O. Lev, *J. Mater. Chem. A*, 2014, **2**, 8431–8437.
- 6 L. Wang, X. He, J. Li, W. Sun, J. Gao, J. Guo and C. Jiang, *Angew. Chem., Int. Ed.*, 2012, **51**, 9034–9037.
- 7 N. Liu, Z. Lu, J. Zhao, M. T. McDowell, H. Lee, W. Zhao and Y. Cui, *Nat. Nanotechnol.*, 2014, **9**, 187–192.
- 8 K. Sumida, D. L. Rogow, J. A. Mason, T. M. McDonald, E. D. Bloch, Z. R. Herm, T. H. Bae and J. R. Long, *Chem. Rev.*, 2012, **112**, 724–781.
- 9 X. X. Li, F. Y. Cheng, S. N. Zhang and J. Chen, *J. Power Sources*, 2006, **160**, 542–547.
- 10 K. Saravanan, M. Nagarathinam, P. Balaya and J. J. Vittal, *J. Mater. Chem.*, 2010, **20**, 8329–8335.
- 11 R. Senthil Kumar, C. Nithya, S. Gopukumar and M. Anbu Kulandainathan, *Energy Technol.*, 2014, **2**, 921–927.
- 12 P. Nie, L. F. Shen, H. F. Luo, B. Ding, G. Y. Xu, J. Wang and X. G. Zhang, *J. Mater. Chem. A*, 2014, **2**, 5852–5857.
- 13 D. Y. Du, J. S. Qin, S. L. Li, Z. M. Su and Y. Q. Lan, *Chem. Soc. Rev.*, 2014, **43**, 4615–4632.
- 14 Y. F. Yue, Y. C. Li, Z. H. Bi, G. M. Veith, C. A. Bridges, B. K. Guo, J. H. Chen, D. R. Mullins, S. P. Surwade, S. M. Mahurin, H. J. Liu, M. P. Paranthaman and S. Dai, *J. Mater. Chem. A*, 2015, **3**, 22989–22995.
- 15 (a) J. S. Qin, D. Y. Du, W. Guan, X. J. Bo, Y. F. Li, L. P. Guo, Z. M. Su, Y. Y. Wang, Y. Q. Lan and H. C. Zhou, *J. Am. Chem. Soc.*, 2015, **137**, 7169–7177; (b) X. J. Yang, M. Sun, H. Y. Zang, Y. Y. Ma, X. J. Feng, H. Q. Tan, Y. H. Wang and Y. G. Li, *Chem. – Asian J.*, 2016, **11**, 858–867.
- 16 H. Wu, J. Yang, Z. M. Su, S. R. Batten and J. F. Ma, *J. Am. Chem. Soc.*, 2011, **133**, 11406–11409.
- 17 D. Y. Du, J. S. Qin, C. G. Wang, X. C. Liu, S. L. Li, Z. M. Su, X. L. Wang, Y. Q. Lan and E. B. Wang, *J. Mater. Chem.*, 2012, **22**, 21040–21044.
- 18 R. S. Kumar, C. Nithya, S. Gopukumar and M. A. Kulandainathan, *Energy Technol.*, 2014, **2**, 921–927.
- 19 (a) H. B. Wang, Q. M. Pan, Y. X. Cheng, J. W. Zhao and G. P. Yin, *Electrochim. Acta*, 2009, **54**, 2851–2855; (b) F. Zhou, S. Xin, H. W. Liang, L. T. Song and S. H. Yu, *Angew. Chem., Int. Ed.*, 2014, **53**, 11552–11556; (c) S. Petnikotaa, S. K. Markaa, V. V. Srikantha, M. V. Reddyb and B. V. Chowdarib, *Electrochim. Acta*, 2015, **178**, 699–708.
- 20 T. Wei, M. Zhang, P. Wu, Y. J. Tang, S. L. Li, F. C. Shen, X. L. Wang, X. P. Zhou and Y. Q. Lan, *Nano Energy*, 2017, **34**, 205–214.
- 21 H. Wang, S. Hamanaka, Y. Nishimoto, S. Irie, T. Yokoyama, H. Yoshikawa and K. Awaga, *J. Am. Chem. Soc.*, 2012, **134**, 4918–4924.